scientific reports

Check for updates

OPEN

Unveiling oxygen vacancy impact on lizardite thermo and mechanical properties

H. Pecinatto[1], Celso R. C. Rêgo[2]✉, W. Wenzel[2], C. A. Frota[4], B. M. S. Perrone[1], Maurício J. Piotrowski[3], Diego Guedes-Sobrinho[5], Alexandre C. Dias[6], Cicero Mota[7], M. S. S. Gusmão[8] & H. O. Frota[8]

Here, we performed a systematic DFT study assisted by the workflow framework SimStack for the mechanical and thermodynamic properties of the clay mineral lizardite in pristine and six different types of O vacancies configurations. In most cases, the defect caused a structural phase transition in the lizardite from the trigonal (pristine) to the triclinic phase. The results show that oxygen vacancies in lizardite significantly reduce the lattice thermal conductivity, accompanied by an elastic moduli reduction and an anisotropy index increase. Through the *P–V* relation, an increase in compressibility was evidenced for vacancy configurations. Except for the vacancy with the same crystalline structure as pristine lizardite, the sound velocities of the other vacancy configurations produce a decrease in these velocities, and it is essential to highlight high values for the Grüneisen parameter. We emphasize the great relevance of the punctual-defects introduction, such as O vacancies, in lizardite, since this microstructural design is responsible for the decrease of the lattice thermal conductivity in comparison with the pristine system by decreasing the heat transfer ability, turning lizardite into a promising candidate for thermoelectric materials

Mineral clays are fascinating geological materials necessary in geophysics and potential technological applications. These materials possess plasticity when interacting with water and transform into ceramics in their absence, with prehistoric records of their applicability. Their structure comprises flat hexagonal sheets, and a serpentine family is a prominent group, with chrysotile, antigorite, and lizardite as the main members. They all have a similar chemical composition: $Mg_3(Si_2O_5)(OH)_4$, composed of Si ion tetrahedrally coordinated with four O atoms and an Al or Mg ion octahedrally coordinated with six O or OH[1], but different structures, depending on the arrangement of the silica-based tetrahedra to the aluminum- or magnesium-based octahedra[2]. Among these, lizardite (space group P31m and trigonal crystal structure[3,4]) is particularly noteworthy due to its abundance, stability under ambient conditions, and quasi-two-dimensional system, which favors its nanotechnology applications[5]. However, further studies are necessary to fully understand its mechanical properties, thermal transport, and thermodynamics in general from a compositional/constitutional understanding point of view.

Lizardite is the product of the metamorphic alteration of ultramafic igneous rocks that results in a crystalline structure that alternates silicate-tetrahedral (corner-shared SiO_4 units) and Mg-octahedral (edge-shared $MgO_2(OH)_4$ octahedra) layers, forming a stacking of 1:1 sheets held together by weak hydrogen bonds. This intriguing structural arrangement, which is prone to volume swelling/shrinkage depending on changes in water content, needs further investigation from a theoretical and experimental point of view. As it is challenging to synthesize lizardite crystals of sufficient size to be used in experimental studies, there have been several theoretical studies based on semi-empirical methods[6] and *ab initio* calculations based on density functional theory (DFT)[7–9]. Such studies focus on addressing structural, elastic, vibrational, and bonding properties, concentrating special attention on the pristine lizardite structure without considering its possible realistic constitution in nature, i.e., the defects in its structure.

[1]PPG-FIS, Federal University of Amazonas, Manaus, AM, Brazil. [2]Karlsruhe Institute of Technology (KIT), Institute of Nanotechnology Hermann-von-Helmholtz-Platz, 76344 Eggenstein-Leopoldshafen, Germany. [3]Department of Physics, Federal University of Pelotas, PO Box 354, Pelotas, RS 96010-900, Brazil. [4]Department of Civil Engineering, Federal University of Amazonas, Manaus, AM, Brazil. [5]Chemistry Department, Federal University of Paraná, Curitiba 81531-980, Brazil. [6]University of Brasília, Institute of Physics, Brasília-DF 70919-970, Brazil. [7]Department of Mathematics, Federal University of Amazonas, Manaus, AM, Brazil. [8]Department of Physics, Federal University of Amazonas, Manaus, AM, Brazil. ✉email: celso.rego@kit.edu

From pristine lizardite studies, Auzende et al.[6] have studied the elastic properties and the interaction energy between layers, as a function of pressure (P) and temperature T, of the hydrous phyllosilicate lizardite, using atomistic calculations and the third-order Birch-Murnaghan expression[10,11], which is an appropriated approach to obtain the silicate[12–14] and phyllosilicates[15–17] crystalline structures and mechanical properties. In complete agreement with Auzende et al.[6], Reynard et al.[7] has obtained the elastic properties of lizardite via DFT at static conditions, where they have got the elastic stiffness constants and elastic compliances constants. On the other hand, Mookherjee and Stixrude[8] performed *ab initio* calculations for lizardite under pressure, where they calculated the elastic stiffness constants and observed that the Birch-Murnaghan equation of state is not appropriate to describe the pressure-volume relationship over the entire range including low (from 0 to 7 GPA), intermediate (from 7 to 22 GPa), and high (greater than 22 GPa) pressure regions. Subsequently, the softening in the c-axis direction was associated with the abrupt decay at 10 GPa of the elastic stiffness constants[18]. Very recently, Deng et al.[9] presented a comprehensive DFT-based study on the lizardite elastic properties at P-T conditions of subduction zones, showing that lizardite has significant shear wave anisotropy and arguing that its large elastic anisotropy could result from the shear-wave splitting in the subducting slabs.

Examining lizardite's natural state is crucial to providing a detailed understanding resulting from myriad interactions and distinct chemical environments. The structural composition of lizardite is influenced by a range of defects, including the presence of trace elements such as (Mn, Fe, Co, Ni, Zn, and Al)[19]. Furthermore, the structure accommodates interstitial H_2O molecules[20–22], and critically, vacancies. Recently, Gusmão et al.[5] employed DFT calculations to scrutinize the impact of Mg cation substitution by Ca, Mn, Fe, Ni, and Zn on lizardite's elastic properties. Their findings revealed noticeable shifts in the mechanical resistance and anisotropy of the resulting compounds compared to pure lizardite. Another noteworthy study by Sun et al.[23] explored the enthalpy formation for H_2O defects during the dehydration process and found substantial alterations in lizardite's elastic properties, affecting seismic velocities and their anisotropy. However, it's important to underscore that there is a considerable gap in the existing literature when it comes to vacancy-type defects in lizardite. Despite the advancements in understanding the material's behavior due to other kinds of defects, vacancy-type defects remain an unexplored avenue, which we try to unravel here.

Considering oxygen-abundance in lizardite composition, the most likely vacancy-type are by oxygen ones, which also happens in perovskite- (ABO_3)[24–28] and scheelite-type (ABO_4, where A and B are cations)[29–31] structures. Thus, the same behavior is expected for lizardite, i.e., the oxygen-vacancy occurrence, because of the crystal growth process, annealing, and/or substitutions inside the crystalline structure, significantly changing these materials' electronic, optical, and mechanical properties. Therefore, we have performed a systematic study on the oxygen-vacancy effects on the lizardite ($Mg_3(Si_2O_5)(OH)_4$) related to their mechanical and thermodynamic properties through the first-principles calculations based on DFT assisted by the workflow framework SimStack, considering lizardite pristine and with oxygen vacancies, for six vacancy-types, aiming to decrease its heat transfer ability, which is associate with better thermoelectric efficiency. From our calculation, we observed that the oxygen vacancies reduce the lattice thermal conductivity of lizardite. Materials with low lattice thermal conductivity are essential for thermoelectric applications. The maximum efficiency in converting heat into electricity by a thermoelectric device is expressed by the figure of merit $ZT = \sigma S^2 T/(\kappa_e + \kappa_L)$, where σ is the electronic conductivity, S is the Seebeck coefficient, T is the temperature and κ_e is the thermal electronic conductivity. Since σ, S, and κ_e are interdependent and vary proportionally, an exciting strategy to enhance ZT is to search for materials with small lattice thermal conductivity κ_L. In this scenario, lizardite with oxygen vacancy can be a good candidate for application in thermoelectric technologies. Section "Methodology" presents the methodology with the atomic configurations, computational method, scientific workflow, and property analyses; Section "Results and discussion" shows the results and discussion; and in the last section, we have the conclusions.

Methodology

Atomic configurations

The $Mg_3(Si_2O_5)(OH)_4$ lizardite structure is a layered trigonal crystal with a space group P31m[3,4] which has been studied in its pristine form and with six different types of oxygen vacancies, for which, we obtained the structural, mechanical, and thermodynamic properties. Following the Kroger-Vink notation[32], we have organized the oxygen vacancies as follows: $V^{\times}_{O1}$ – formed by removing one (basal) O atom that bonds to two Si atoms in the tetrahedra layer; $V^{\times}_{O2}$ – by removing one (apical) O atom that bonds to a Si atom in the tetrahedra layer with three Mg atoms in the octahedra layer; $V^{\times}_{O3}$ – by removing one OH from the top of the octahedra layer; the double vacancies: $V^{\times}_{O1\text{-}O2}$, $V^{\times}_{O1\text{-}O3}$, and $V^{\times}_{O3\text{-}O3}$ are originated from the simultaneous formation of the vacancy pairs: $V^{\times}_{O1}$ & $V^{\times}_{O2}$, $V^{\times}_{O1}$ & $V^{\times}_{O3}$, and $V^{\times}_{O2}$ & $V^{\times}_{O3}$, respectively. For clarity, Fig. 1 can be consulted to differentiate the six types of oxygen vacancies (top) and for a more precise notion of the layered lizardite structure (bottom).

Total energy calculations

Our *ab initio* calculations are based on DFT, as implemented in the Quantum ESPRESSO (QE) package[33], using the ultrasoft method[34] within the generalized gradient approximation with the semilocal Perdew–Burke–Ernzerhof (PBE)[35] formulation for the exchange-correlation energy functional. As DFT-PBE cannot provide an accurate description of the nonlocal long-range van der Waals (vdW) interactions, we employ the vdW D2 correction proposed by Grimme[36,37], which possess a good compromise between accuracy and computational coast[38,39]. The geometry optimization was carried out by the Broyden–Fletcher–Goldfarb–Shanno (BFGS) quasi-Newton algorithm[35], with the convergence thresholds on forces and total energy for ionic minimization established in 10^{-6} eV/Å and 10^{-5} eV, respectively. The kinetic energy cutoffs related to the wave functions and charge density calculations in the summation were 0.8 keV and 8.2 keV, respectively. After convergence tests, a Monkhorst-Pack

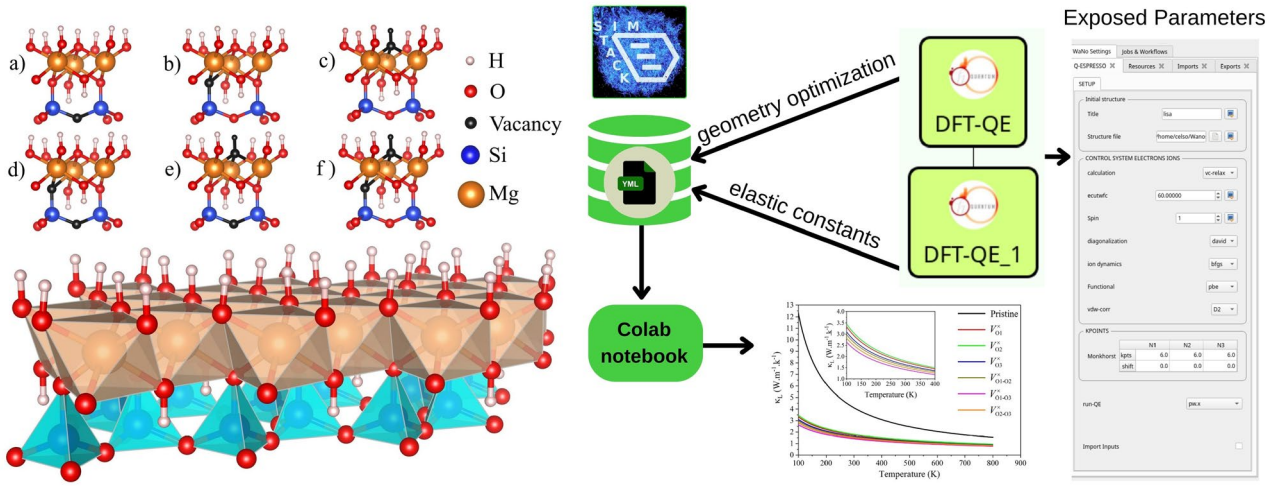

Figure 1. Left bottom: $Mg_3(Si_2O_5)(OH)_4$ one-layer representation, consisting of two sheets: an octahedra sheet, with Mg atom at the center of the octahedron; over a tetrahedra sheet, with Si atom at the center of the tetrahedron. Each Mg (Si) atom is surrounded by six (four) O atoms, and the atomic site on the octahedron top is occupied by OH. Top: the six types of oxygen vacancies: (**a**) removal of one (basal) O atom that bonds two Si atoms at the base of the tetrahedra sheet ($V^{\times}_{O1}$); (**b**) elimination of one (apical) O atom that bonds one Si atom in the tetrahedra sheet with three Mg atoms in the octahedra sheet ($V^{\times}_{O2}$); (**c**) elimination of one OH from the top of the octahedra sheet ($V^{\times}_{O3}$); (**d**) double vacancy originated from the simultaneous $V^{\times}_{O1}$ & $V^{\times}_{O2}$ vacancies ($V^{\times}_{O1\text{-}O2}$); (**e**) double vacancy originated from the simultaneous $V^{\times}_{O1}$ & $V^{\times}_{O3}$ vacancies ($V^{\times}_{O1\text{-}O3}$); and (**f**) double vacancy originated from the simultaneous $V^{\times}_{O2}$ & $V^{\times}_{O3}$ vacancies ($V^{\times}_{O2\text{-}O3}$). On the right side: We display the workflow that we used to do all the simulations and calculate the properties of Lizardite. In the steps DFT-QE and DFT-QE_1, we optimized geometry and the elastic constants. These steps created a database that we then fed into a Colab notebook to calculate lattice thermal conductivity (κ_L).

scheme was used for the Brillouin zone integration, with a $6 \times 6 \times 6$ **k**-point mesh. The graphical representations of the structural models were performed using the VESTA package[40].

SimStack workflow

SimStack[41] is a robust workflow framework that ensures the reproducibility and transferability of the simulation protocols[42]. Additionally, it simplifies the creation of custom-tailored simulation protocols using various computer simulation approaches. Here we use the Workflow Active Node (WaNo) DFT-QE[43], which saves time by automating and reducing protocol complexity, permitting the monitoring of multiple sets of calculations for independent DFT protocols for different Lizardite configurations. The right side of Fig. 1 depicts this workflow, streamlining the optimization and elastic constants calculations using QE code. The output of DFT simulations for each Lizardite system automatically generates *.yml* file database, which we automatically may transfer to a Colab notebook to query data and calculate the lattice thermal conductivity κ_L. To meet the FAIR principles[44], we make all input data and the Colab notebook available on the following repository github.com/KIT-Workflows/Lizardite.

Property analyses

To deepen the understanding of lizardite, we have systematically analyzed its main mechanical and thermodynamic properties, including the lattice thermal conductivity. Further details on the properties are provided in the Supporting Information (SI) material. In terms of mechanical properties, we had considered the elastic stiffness (c_{ij}) and compliance (s_{ij}) constants (and their relations) as implemented in the Thermo_pw package[45], checking the stability criterion when the eigenvalues of the elastic stiffness matrix were greater than zero[46–49]. Posteriorly, assuming the relaxation process under hydrostatic pressure[50], the Voigt and Reuss bulk (B_V, B_R) and shear (G_V, G_R) moduli, respectively, were obtained from c_{ij} and s_{ij}. From which, the Hill bulk (B_H) and shear (G_H) moduli are given by averaging the corresponding values[50]: $B(G)_H = 1/2(B(G)_V + B(G)_R)$. Considering Hill's modulus and the mathematical theory of elasticity[51], the Young's modulus (E_H) and Poisson's ratio (ν_H) were also considered. At the same time, the anisotropy of the material was obtained from the universal elastic anisotropy index (A^U)[52]. Finally, we also have the possibility of estimating the ductility or brittleness of material through the criterion suggested by Pugh[53], for which ratios B_H/G_H larger than 1.75 represent a ductile material.

Considering a P–V equations of state, the thermodynamic properties were obtained from the structural relaxation process under a pressure range from 0.0 to 8.0 GPa. The isochoric heat capacity (C_V) was achieved by post-processing with Thermo_pw package[45], considering the Debye temperature (Θ_D) within the Debye model. To get Θ_D, the elastic constant data was considered through the Voigt–Reuss–Hill average of the bulk and shear moduli to calculate the average sound velocities. Following Anderson[54], where Θ_D depends on the average sound velocity (v_{av}), which is given in terms of the longitudinal (v_ℓ) and transverse (v_t) sound velocities,

i.e., $v_{av} = [1/3(1/v_\ell^3 + 2/v_t^3)]^{-1/3}$. In turn, v_ℓ and v_t depends on the mechanical properties (B_H and G_H)[51,55]. Similarly, the Grüneisen acoustic constant (γ) was calculated as a v_ℓ and v_t function, following Belomestnykh[56]. See more details about thermodynamic properties in SI.

For the lattice thermal conductivity (κ_L), we have considered two models: (*i*) for the pristine lizardite, the Slack model[57,58] has been adopted since it is widely appropriated for defect-free crystals and lattice thermal resistance resulting only from intrinsic phonon-phonon interactions[59–62]. The κ_L is obtained from Θ_D and γ, which can be obtained from lattice dynamic calculations or experimental measurements[57,61]. However, in the present work, we have obtained κ_L considering directly the Θ_D and γ calculation (see SI for mathematical expressions), in complete agreement with Xia et al.[63] approach. (*ii*) For lizardite with oxygen vacancies, κ_L is calculated following the seminal works of Klemens[64,65] and corroborated by Callaway et al.[66] and Abeles[67]. Basically, κ_L for lizardite with an oxygen vacancy type ($V_\alpha^\times$) is defined as $\kappa_{V_\alpha^\times} = \kappa_L[(\tan^{-1} u)/u]$, i.e., it is given in terms of κ_L for the pristine lizardite and u is written as a function of Θ_D, κ_L, v_{av}, and Γ (which is given in terms of the concentration and mass of the atom type *i*). Finally, the minimum lattice thermal conductivity of lizardite with oxygen vacancy ($\kappa_{V_\alpha^\times(\min)}$) is obtained using the minimum value of κ_L for pristine lizardite ($\kappa_{L(\min)}$), according to Clarke[68]. More details are presented in the SI material.

In Table 1 we present the accuracy of the Belomestnykh approximation used in the present work to determine the Grüneisen parameters, in relation to the DFT calculation , for some examples from literature for structure simpler than the lizardite one. It is observed that the results from the Belomestnykh approach are in reasonable agreement with the DFT calculations.

Results and discussion

Geometric optimization

We have performed the structural optimization of pristine and oxygen vacancies lizardite within the stacking layer context, each of which is composed of two sheets: a Mg-centered octahedra over a Si-centered tetrahedra sheet, as shown in the bottom of Fig. 1. The six types of O-vacancies considered are given by: $V_{O1}^\times$, $V_{O2}^\times$, $V_{O3}^\times$, $V_{O1\text{-}O2}^\times$, $V_{O1\text{-}O3}^\times$, and $V_{O2\text{-}O3}^\times$, as shown at the top of Fig. 1 (from a) to f), respectively). The structural relaxation procedure of these systems and the subsequent comparison between the pristine and defect systems are of great relevance for establishing the main structural changes resulting from vacancy formation. Thus, the main structural properties discussed here, e.g., lattice parameters (a, b, c), angles (α, β, γ), volume, density, and interlayer distance, are also presented in SI (Table S1).

For the pristine lizardite, we have obtained a trigonal lattice with parameters: $a = b = 5.276$ Å and $c = 7.117$ Å; $\alpha = \beta = 90°$ and $\gamma = 120°$, and a layer distance of 1.783 Å, results that are in excellent agreement with previous works[5]. The formation of different types of vacancies in lizardite can lead to further structural parameter responses. In this context, we initially estimated the formation viability of the O-vacancies studied based on the formation energy (ΔE_v^o) as established by Emery and Wolverton[72]:

$$\Delta E_v^o = E(Mg_3Si_2O_{(5-\alpha)}(OH)_{(4-\beta)}) + \alpha\mu_O + \beta\mu_H - E(Mg_3Si_2O_5(OH)_4), \quad (1)$$

where $E(Mg_3Si_2O_{(5-\alpha)}(OH)_{(4-\beta)})$ is the total energy of $Mg_3Si_2O_5(OH)_4$ with vacancy, μ_O and μ_H are the O and H chemical potentials, respectively, $E(Mg_3Si_2O_5(OH)_4)$ is the total energy of the pristine $Mg_3Si_2O_5(OH)_4$, and α (β) is the number of O atoms removed from a tetrahedron vertex (the top of the octahedra sheet), and zero otherwise. The ΔE_v^o values, along with the percentage differences in the volume (ΔVol) and interlayer distance (Δid) concerning the pristine system, are shown in Table 2.

From Table 2, it is observed that the lowest formation energy is obtained for $V_{O2}^\times$ vacancy-type, followed by $V_{O1}^\times$ and $V_{O3}^\times$. In contrast, the formation energy of a double vacancy is approximately the sum of the energies of the two single vacancies that originated it. This result is directly associated with the fact that only $V_{O2}^\times$ preserved the trigonal lattice structure in agreement with the pristine lizardite. At the same time, the other vacancy systems changed the lattice structure type from trigonal to triclinic. For $V_{O2}^\times$, the removal of an oxygen atom between the octahedra and tetrahedra sheets causes a moderate volume contraction ($\Delta Vol = -2.67\%$), which is directly linked to an approximation between the sheets ($\Delta id = -5.89\%$) concerning pristine lizardite, all without changing the lattice angles of the trigonal structure. On the other hand, all different vacancy types represent structural

Compound	γ (DFT)	γ(Belomestnykh)
Mg_3Sb_2	1.83[(a)]	1.85[(a)]
$CaMg_2Sb_2$	1.44[(a)]	1.40[(a)]
$CaMg_2Bi_2$	1.46[(a)]	1.45[(a)]
Bi_2Te_3	1.52[(b)]	1.65[(c)]
SnSe	2.83[(d)]	3.13[(d)]
PbTe	1.49[(d)]	1.65[(d)]
PbSe	2.66[(d)]	1.69[(d)]
PbS	2.46[(d)]	1.67[(d)]

Table 1. Comparision of the Grüneisen parameters obtained from the Belomestnykh approximation with the DFT calculation for some compounds.. (a) Ref.[69] (b) Ref.[70] (c) Ref.[71] (d) Ref.[63]

Vacancy	$V^{\times}_{O1}$	$V^{\times}_{O2}$	$V^{\times}_{O3}$	$V^{\times}_{O1\text{-}O2}$	$V^{\times}_{O1\text{-}O3}$	$V^{\times}_{O2\text{-}O3}$
ΔE^{o}_{v} (eV)	0.824	0.773	0.874	1.592	1.665	1.665
ΔVol (%)	− 4.83	− 2.67	0.39	− 6.45	− 5.20	− 2.75
Δid (%)	− 2.36	− 5.89	− 0.17	− 9.48	− 7.12	− 8.02

Table 2. The formation energy of O vacancy per oxygen atom (ΔE^{o}_{v}), the percentage difference in the volume of structures concerning the pristine one (ΔVol), and the percentage difference in the interlayer distance (Δid) for the pristine system, for different types of vacancies in lizardite. Negative (positive) ΔVol and Δid values represent a decrease (increase) in the volume and interlayer distance of the structures with pristine lizardite..

changes in the pristine lizardite that, to a greater or lesser extent, lead to distortions that penalize the stabilization of the system with point defects, with volume variations ranging from a slight expansion ($\Delta Vol = 0.39\%$) for $V^{\times}_{O3}$, due to the small approximation between the sheets ($\Delta id = -0.17\%$), to significant volume contractions ($\Delta Vol = -6.45\%$) for $V^{\times}_{O1\text{-}O2}$, due to the largest approximation between sheets ($\Delta id = -9.48\%$), all of them within the structural context of the triclinic lattice. In short, the six vacancy types studied here represent, together with pristine lizardite, a very diversified set from the point of view of possible structural alterations. At the same time, they are energetically viable possibilities to happen in a practical application.

Mechanical properties

We started the study of the mechanical properties of pristine and vacancy-type lizardite from the calculation of the elastic stiffness constants c_{ij} and the elastic compliances constants s_{ij}, which are presented in the SI (Table S2). From this, we performed a two-level characterization of the main mechanical properties, a primary and complementary description of the mechanical response properties of the studied materials. Firstly, from the matrices $[c_{ij}]$ and $[s_{ij}]$, it is possible to check the mechanical stability criterion, which establishes that all eigenvalues of these matrices must be greater than zero to achieve the elastic stability[46–49]. All structures studied here meet this criterion, showing elastic stability in pristine and vacancy-type constitutions. Our results are in excellent agreement with the literature for the case of pristine lizardite[8].

Within the context of basic mechanical properties, we can check on (*i*) the in-plane and out-of-plane mechanical stiffness, (*ii*) the fracture resistance (or rigidity), and (*iii*) the stress anisotropy of the lizardite configurations with and without defect, which turns out to be interesting in the scenario of how pristine and vacancy-types lizardite resists concerning the stress application. For (*i*), an estimate can be made through the ratio c_{11}/c_{33}, whose values are presented in Table 3. We obtain a ratio $c_{11}/c_{33} = 1.707$ for the pristine configuration, which implies a greater mechanical stress resistance in-plane than out-of-plane. As expected, for configurations with vacancy, we have a stiffness dependence on the sites from which the O atom has been removed. Except for $V^{\times}_{O1\text{-}O3}$, for which the in-plane and out-of-plane stiffness are equivalent, all other cases of vacancy cases behave like the pristine lizardite, i.e., are weaker bonds along the [001] direction. For (*ii*), the estimate is made by the ratio c_{66}/c_{44}, which represents how much the basal plane is more resistant to fracture than the axis perpendicular to this plane when shear stress is applied. The rigidity values (c_{66}/c_{44}) are presented in Table 3. We observed that, with pristine lizardite, the basal plane is more (less) resistant to fractures than the c-axis for $V^{\times}_{O1}$, $V^{\times}_{O3}$, $V^{\times}_{O1\text{-}O3}$ and $V^{\times}_{O2\text{-}O3}$ ($V^{\times}_{O2}$ and $V^{\times}_{O1\text{-}O2}$). Finally, for (*iii*), we can estimate the stress anisotropy from the linear compressibility (β), which represents the relative variation in the length of a line when the body is subjected to unit hydrostatic pressure[73] and depends on the elastic compliance constants s_{ij}. Following the Nye work[49], we have estimated β for trigonal and triclinic crystal systems in each axial direction, as follows: $\beta_1 = s_{11} + s_{12} + s_{13}$ (both), $\beta_2 = \beta_1$ (trigonal), $\beta_2 = s_{12} + s_{22} + s_{23}$ (triclinic), $\beta_3 = 2s_{13} + s_{33}$ (trigonal), and $\beta_3 = s_{13} + s_{23} + s_{33}$ (triclinic). The β values are also presented in Table 3, in which we observe that the two configurations with trigonal lattice (pristine and $V^{\times}_{O2}$) present isotropic in-plane stiffness ($\beta_1 = \beta_2$) as expected, due to the crystalline symmetry. In contrast, the other vacancy-types lizardite configurations show planar anisotropy.

Compound	c_{11}/c_{33}	c_{66}/c_{44}	β_1	β_2	β_3
Pristine	1.707	3.630	0.247	0.247	0.607
$V^{\times}_{O1}$	1.650	6.120	0.349	0.306	0.792
$V^{\times}_{O2}$	1.440	3.380	0.275	0.275	0.541
$V^{\times}_{O3}$	2.050	7.370	0.324	0.351	1.061
$V^{\times}_{O1\text{-}O2}$	1.190	3.570	0.458	0.347	0.652
$V^{\times}_{O1\text{-}O3}$	0.990	3.730	0.687	0.489	0.957
$V^{\times}_{O2\text{-}O3}$	1.740	4.170	0.367	0.310	0.891

Table 3. The in-plane and out-of-plane mechanical stiffness (c_{11}/c_{33}), fracture resistance (c_{66}/c_{44}), and linear compressibilities (β_1, β_2, and β_3) of the lizardite with and without O vacancies. The linear compressibilities are given in 1/Mbar=1/100GPa..

Complementarily, using the elastic constants tensor and the Voigt, Reuss, and Hill models, we have obtained the bulk (B_V, B_R), shear (G_V, G_R), and Young (E_H) moduli, as well as the Poisson's ratio (ν_H) and the universal elastic anisotropy index (A^U) for a complete mechanical property characterization of the pristine lizardite and with different O vacancy-types. All these properties are shown in Table 4. First, we observe that the vacancy formation leads to a decrease in the B_V, B_R, G_V, G_R, and E_H values, which is directly associated with the degree of the constitutional importance of the O atom(s) removed to form the vacancy. For example, the smallest elastic modulus values occur for a double vacancy, specifically for $V^{\times}_{O1\text{-}O3}$, when two O atoms are removed, one bonded to two Si atoms at the base of the tetrahedra sheet and the other at the top of the octahedra sheet. Even more specifically, the $V^{\times}_{O3}$ vacancy type leads to elastic moduli smaller than $V^{\times}_{O1}$ one, i.e., removing a O atom from the top of the octahedra sheet decreases the elastic moduli more than removing a O atom from the base of the tetrahedra sheet. All studied configurations prefer to be shear deformed since the shear moduli are smaller than the bulk moduli. In the case of the ν_H values, we observed a slight variation ($\nu_H = 0.30 \pm 0.01$). Similarly to the small variation of the ratio B_H/G_H, i.e., between 2.01 and 2.24, which, according to the criterion suggested by Pugh[53], characterizes all our configurations as ductile, since the values are more significant than 1.75. Finally, the smallest A^U values occur for the trigonal structures (pristine and $V^{\times}_{O2}$), which are isotropic in-plane in terms of stiffness, in contrast to triclinic (all other cases), in complete agreement with the linear compressibility results.

Thermodynamic properties

Once the mechanical properties of pristine and vacancy-types lizardite were established, there is a need for a thermodynamic property analysis taking into account pressure and temperature variations to trace the real implications of O vacancies in the lizardite constitution. First, in terms of the pressure variation, we obtained the P–V equations of state from the structural relaxation under pressure (from zero to 8.0 GPa), which are presented in Fig. 2. The normalized volume (relative to the structure at zero pressure) decreases with increasing pressure for all configurations, and the P–V curve shows a greater slope with O vacancies, i.e., the lizardite configurations with vacancies present a more significant decrease in volume with increasing pressure, which is directly correlated with the mechanical properties elucidated by the bulk, shear, and Young modulus values (see Table 4). Up to 4.5 GPa, the P–V curves of the pristine and $V^{\times}_{O2}$ configurations have the same response to pressure increase, keeping in mind that both have the trigonal crystalline structure; for values larger than 4.5 GPa, we observe that the $V^{\times}_{O2}$ configuration starts to have a more accentuated response to the pressure increase, which is associated with the structural change that is evident from the lattice parameters (a and c) variation in the insert of Fig. 2. All other configurations with vacancy, possessing the triclinic crystalline structure, are more susceptible to pressure variations, respond more accentuated, and are more compressible. The most significant decrease in volume with the pressure increase occurs for $V^{\times}_{O1\text{-}O3}$ and $V^{\times}_{O2\text{-}O3}$ (whose P–V diagrams are practically overlapping), which are the two configurations with double vacancies that have the highest (and identical) vacancy formation energies. These three lizardite configurations ($V^{\times}_{O2}$, $V^{\times}_{O1\text{-}O3}$, and $V^{\times}_{O2\text{-}O3}$) had a change in the expected linear behavior between volume and pressure, showing an increase in the slope from 4.5 GPa, which is associated with the rise in compressibility that occurs mainly on the c axis, which implies a reduction in the interlayer space and significant changes in the O–H–Mg angle, positioning O–H outside the normal direction.

For the temperature variation, we performed the isochoric heat capacity (C_V) calculation, which first requires obtaining Θ_D from the Debye model, whose expression depends on v_{av}, given by the angular average of the sound velocities calculated for each propagation direction, i.e., v_ℓ and v_t, both being important for the Grüneisen acoustic constant (γ) determination. Thus, before we get into C_V, we briefly discuss the v_ℓ, v_t, v_{av}, γ, and Θ_D results for lizardite configurations with and without vacancies, as presented in Table 5. Our sound velocity results are in excellent agreement with the experimental results obtained for pristine lizardite. For example, Kern et al.[74] have obtained v_ℓ and v_t in the serpentine, at low pressure, around 7.2 and 4.8 km/s, respectively. According to Christensen[75], which presented v_ℓ values in the range of 5.0–8.3 km/s, depending on the sample serpentinization. Or the work by Seipold and Schilling[21], for which v_{av} varies from approximately 5.02 km/s under ambient conditions to 4.5 km/s at 900 K.

From Table 5, we observe that, in general, the different vacancy-types formation is associated with a sound velocity decrease, except for the pristine and $V^{\times}_{O2}$ configurations, the only vacancy configuration that preserves

Compound	B_V	G_V	B_R	G_R	E_H	ν_H	A^U
Pristine	101.84	53.45	90.85	35.74	115.64	0.30	2.60
	(95.66)	(53.85)	(80.70)	(36.23)	(115.46)	(0.28)	(2.63)
$V^{\times}_{O1}$	79.71	47.89	69.06	23.96	92.06	0.29	5.15
$V^{\times}_{O2}$	97.57	50.81	91.59	35.73	112.37	0.30	2.18
$V^{\times}_{O3}$	70.85	39.76	57.59	19.88	76.99	0.30	5.23
$V^{\times}_{O1\text{-}O2}$	73.02	42.76	68.63	27.75	90.34	0.29	2.77
$V^{\times}_{O1\text{-}O3}$	57.44	31.59	46.87	15.08	60.47	0.31	5.70
$V^{\times}_{O2\text{-}O3}$	74.78	40.11	63.81	23.26	82.15	0.30	3.80

Table 4. The bulk (B_V, B_R), shear (G_V, G_R), and Young (E_H) moduli (in GPa); the Poisson's ratio (ν_H) and the universal elastic anisotropy index (A^U) of the lizardite with and without vacancies, where the subscript-labels: V, R, and H refer to the Voigt, Reuss, and Hill models, respectively. In parentheses, we have added the respective property values of the pristine lizardite from literature[8].

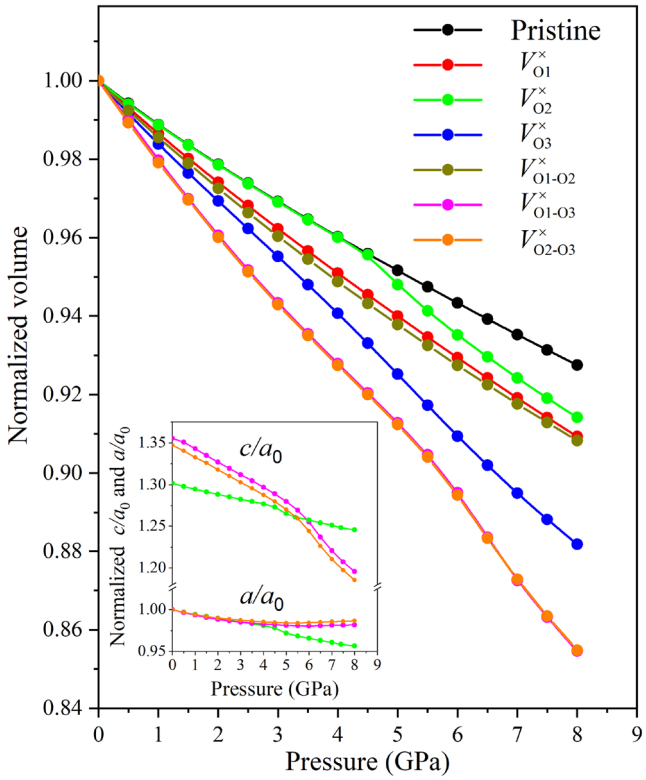

Figure 2. Variation of normalized volume in relation to pressure for pristine and O vacancy-types lizardite. Two inserts are shown for the normalized (scaled by a_0, which consists of a at zero pressure) lattice parameters (a and c) variation in relation to pressure to explain the escape from a linear behavior for the P–V diagrams of the $V^{\times}_{O2}$, $V^{\times}_{O1\text{-}O3}$, and $V^{\times}_{O2\text{-}O3}$ configurations.

Compound	v_ℓ (km/s)	v_t (km/s)	v_{av} (km/s)	v_ℓ/v_t	γ	θ_D (K)	κ_{min} (W/(mK))
Pristine	7.62	4.08	4.55	1.87	1.77	639.60	1.75
$V^{\times}_{O1}$	6.79	3.68	4.10	1.84	1.72	574.91	0.63
$V^{\times}_{O2}$	7.66	3.08	4.56	1.88	1.78	634.09	0.67
$V^{\times}_{O3}$	6.44	3.45	3.85	1.87	1.77	519.40	0.55
$V^{\times}_{O1\text{-}O2}$	6.82	3.73	4.16	1.83	1.69	574.00	0.51
$V^{\times}_{O1\text{-}O3}$	5.78	3.06	3.42	1.89	1.81	460.11	0.40
$V^{\times}_{O2\text{-}O3}$	6.78	3.61	4.04	1.88	1.78	538.19	0.46

Table 5. Longitudinal (v_ℓ), transverse (v_t), and average (v_{av}) sound velocities; the ratio velocities (v_ℓ/v_t); Grüneisen parameter (γ); the Debye temperature (θ_D); and te the minimum thermal conductivity (κ_{min}), of the pristine and O vacancy-types lizardite..

the trigonal crystalline structure. Unanimously, we found that v_ℓ is a bit more than 1.8 times v_t, which means that sound easily propagates in the plane of the layers than along the direction of the stacking layers ([001]). Our v_ℓ/v_t results agree with the experimental results of Christensen[75], by which this ratio increases systematically from 1.78 to 2.21 with increasing sample serpentinization. We correlate the mechanical properties (Table 4) and the sound velocities. For example, $V^{\times}_{O1\text{-}O3}$ has the lowest sound velocities in correspondence to the smallest volume, shear modulus, and Young's modulus. For γ, we observed a slight variation among configurations, leading to an average value of 1.76. On the other hand, Θ_D presents smaller values for the structures with vacancy, being the smallest values for the configurations with a triclinic crystalline lattice than with a trigonal one.

After these preliminary calculations, we performed the C_V calculations concerning the temperature, from 0 to 800 K, for the lizardite configurations with and without O vacancies, which are presented in Fig. 3a. We observed the same behavior trend in the C_V *versus* temperature curves for all lizardite configurations, with an exponential increase in C_V up to approximately room temperature and subsequent logarithmic growth for C_V

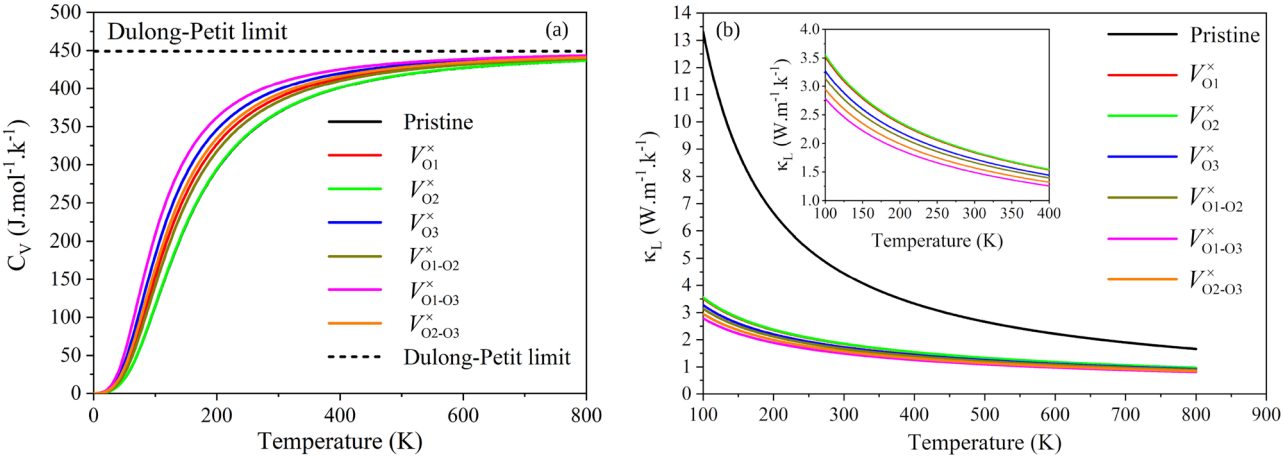

Figure 3. (**a**) The isochoric heat capacity (C_V) of pristine and O vacancy-types lizardite as a function of temperature. (**b**) The lattice thermal conductivity (κ_L) as a temperature function of pristine and O vacancy-types lizardite.

at higher temperatures, with a trend asymptotic to converge to the Dulong-Petit limit at high temperatures. The most significant C_V differences among the configurations occur in the 100–300 K interval, where we observe that, with the $V^{\times}_{O2}$ exception, the C_V values are more prominent for the lizardite configurations with vacancy than that for pristine lizardite.

Lattice thermal conductivity

From γ and Θ_D, we can calculate the lattice thermal conductivity (κ_L), as well as the minimum thermal conductivity (κ_{min})), which are shown in Table 5, for the pristine and O vacancy-types lizardite. The behavior trend between κ_L and κ_{min} is the same across the configurations studied, i.e., for κ_{min} (in W/(m.K)): pristine (1.75) > $V^{\times}_{O2}$ (0.67) > $V^{\times}_{O1}$ (0.63) > $V^{\times}_{O3}$ (0.55) > $V^{\times}_{O1-O2}$ (0.51) > $V^{\times}_{O2-O3}$ (0.46) > $V^{\times}_{O1-O3}$ (0.40), in agreement with κ_L as a temperature function, in Fig. 3b. As evidenced, the O vacancies formation in lizardite leads to a decrease in heat transfer ability compared to the pristine configuration.

Thus, from Fig. 3b, we observe that the O vacancies produce a significant κ_L decrease, following the sound velocities (Table 5), which represents our main result here, since the κ_L values, the material conducts less heat energy. Furthermore, we highlight that this important thermoelectric parameter, directly linked to determining the energy conversion efficiency of thermoelectric materials, has a very low variation with increasing temperature for systems with the vacancy in contrast to the pristine system. Consequently, the introduction of the defect (O vacancies) in lizardite is part of the successful strategy of intelligent microstructural design, which plays an essential role in the task of obtaining materials with high phonon-phonon scattering rates, i.e., materials with significant Grüneisen parameters. These behavior are in agreement with the results obtained by Shen et al.[76] and Jia et al.[77], which studied the effect of vacancies on the lattice thermal conductivity of $CuGaTe_2$ and In_2Te_3 -InSb, respectively.

Conclusions

In the present work, we performed a systematic first-principles study, based on DFT, for the main mechanical and thermodynamic properties of the clay mineral lizardite in pristine and six different types of O vacancies configurations. After the structural relaxation process, except for a vacancy configuration, we obtained a change in the crystalline structure of the vacancy configurations, going from trigonal (pristine) to triclinic. As the main result found, we highlight that oxygen vacancies in lizardite significantly reduce the lattice thermal conductivity, accompanied by an elastic moduli reduction and an anisotropy index increase. Through the *P*–*V* relation, an increase in compressibility was evidenced for vacancy configurations. Except for the vacancy with the same crystalline structure as pristine lizardite, the sound velocities of the other vacancy configurations produce a decrease in these velocities, and it is essential to highlight high values for the Grüneisen parameter. Finally, we emphasize the great relevance of the punctual-defects introduction, such as O vacancies, in lizardite, since this intelligent microstructural design procedure is responsible for the decrease of the lattice thermal conductivity in comparison with the pristine system, which decreases the heat transfer ability, giving rise to an essential candidate for thermoelectric materials.

Data availibility

The data sets used and/or analyzed during the current study are available on the following repository github.com/KIT-Workflows/Lizardite.

Received: 25 May 2023; Accepted: 8 October 2023
Published online: 11 October 2023

References

1. Bergaya, F. & Lagaly, G. *Handbook of Clay Science*, vol. 5 (Elsevier, 2013).
2. Rinaudo, C., Gastaldi, D. & Belluso, E. Characterization of chrysotile, antigorite and lizardite by ft-raman spectroscopy. *Can. Mineral.* **41**, 883–890 (2003).
3. Mellini, M. The crystal structure of lizardite 1T:Hydrogen bonds and polytypism. *Am. Mineral.* **67**, 587–598 (1982).
4. Bard, D., Yarwood, J. & Tylee, B. Asbestos fibre identification by raman microspectroscopy. *J. Raman Spectrosc.* **28**, 803–809 (1997).
5. Gusmão, M. S., Ghosh, A., Siloi, I., Fornari, M. & Nardelli, M. B. Tuning the electronic and magnetic properties of lizardite clay by chemical substitution. *Mol. Syst. Des. Eng.* **7**, 1154–1161 (2022).
6. Auzende, A.-L., Pellenq, R.-M., Devouard, B., Baronnet, A. & Grauby, O. Atomistic calculations of structural and elastic properties of serpentine minerals: The case of lizardite. *Phys. Chem. Miner.* **33**, 266–275 (2006).
7. Reynard, B., Hilairet, N., Balan, E. & Lazzeri, M. Elasticity of serpentines and extensive serpentinization in subduction zones. *Geophys. Res. Lett.***34** (2007).
8. Mookherjee, M. & Stixrude, L. Structure and elasticity of serpentine at high-pressure. *Earth Planet. Sci. Lett.* **279**, 11–19 (2009).
9. Deng, X., Luo, C., Wentzcovitch, R. M., Abers, G. A. & Wu, Z. Elastic anisotropy of lizardite at subduction zone conditions. *Geophys. Res. Lett.* **49**, e2022GL099712 (2022).
10. Birch, F. Finite elastic strain of cubic crystals. *Phys. Rev.* **71**, 809 (1947).
11. Murnaghan, F. D. The compressibility of media under extreme pressures. *Proc. Natl. Acad. Sci.* **30**, 244–247 (1944).
12. Archer, T. *et al.* An interatomic potential model for carbonates allowing for polarization effects. *Phys. Chem. Miner.* **30**, 416–424 (2003).
13. Dove, M. T. *et al.* On the role of al-si ordering in the cubic-tetragonal phase transition of leucite. *Am. Mineral.* **78**, 486–492 (1993).
14. Post, J. E. & Burnham, C. W. Modeling tunnel-cation displacements in hollandites using structure-energy calculations. *Am. Mineral.* **71**, 1178–1185 (1986).
15. Collins, D. R. & Catlow, C. R. A. Computer simulation of structures and cohesive properties of micas. *Am. Mineral.* **77**, 1172–1181 (1992).
16. Sainz-Diaz, C., Hernandez-Laguna, A. & Dove, M. Modeling of dioctahedral 2: 1 phyllosilicates by means of transferable empirical potentials. *Phys. Chem. Miner.* **28**, 130–141 (2001).
17. Teppen, B. J., Rasmussen, K., Bertsch, P. M., Miller, D. M. & Schäfer, L. Molecular dynamics modeling of clay minerals. 1. gibbsite, kaolinite, pyrophyllite, and beidellite. *J. Phys. Chem. B* **101**, 1579–1587 (1997).
18. Tsuchiya, J. A first-principles calculation of the elastic and vibrational anomalies of lizardite under pressure. *Am. Mineral.* **98**, 2046–2052 (2013).
19. Rajkumar, M., Vara Prasad, M. N., Freitas, H. & Ae, N. Biotechnological applications of serpentine soil bacteria for phytoremediation of trace metals. *Crit. Rev. Biotechnol.* **29**, 120–130 (2009).
20. Brindley, G. & Zussman, J. A structural study of the thermal transformation of serpentine minerals to forsterite. *Am. Mineral.* **42**, 461–474 (1957).
21. Seipold, U. & Schilling, F. Heat transport in serpentinites. *Tectonophysics* **370**, 147–162 (2003).
22. Dlugogorski, B. Z. & Balucan, R. D. Dehydroxylation of serpentine minerals: Implications for mineral carbonation. *Renew. Sustain. Energy Rev.* **31**, 353–367 (2014).
23. Sun, S. & He, Y. First-principles investigations on the formation of H_2O defects in lizardite with influence on the elastic property. *Phys. Chem. Miner.* **46**, 935–946 (2019).
24. Inzani, K., Grande, T., Vullum-Bruer, F. & Selbach, S. M. A van der waals density functional study of MoO_3 and its oxygen vacancies. *J. Phys. Chem. C* **120**, 8959–8968 (2016).
25. Albanese, E., Di Valentin, C. & Pacchioni, G. H_2O adsorption on WO_3 and WO_{3-x} (001) surfaces. *ACS Appl. Mater. Interfaces* **9**, 23212–23221 (2017).
26. Tahini, H. A. *et al.* Mobile polaronic states in α-MoO_3: An ab initio investigation of the role of oxygen vacancies and alkali ions. *ACS Appl. Mater. Interfaces* **8**, 10911–10917 (2016).
27. Ribeiro, R., Longo, E., Andres, J. & de Lazaro, S. R. A DFT investigation of the role of oxygen vacancies on the structural, electronic and magnetic properties of $ATiO_3$ (A= Mn, Fe, Ni) multiferroic materials. *Phys. Chem. Chem. Phys.* **20**, 28382–28392 (2018).
28. Zhang, Y., Wang, J., Sahoo, M., Shimada, T. & Kitamura, T. Mechanical control of magnetism in oxygen deficient perovskite $SrTiO_3$. *Phys. Chem. Chem. Phys.* **17**, 27136–27144 (2015).
29. Yuan, Y., Huang, Y., Ma, F., Zhang, Z. & Wei, X. Effects of oxygen vacancy on the mechanical, electronic and optical properties of monoclinic $BiVO_4$. *J. Mater. Sci.* **52**, 8546–8555 (2017).
30. Luo, F. *et al.* Engineering oxygen vacancies of cobalt tungstate nanoparticles enable efficient water splitting in alkaline medium. *Appl. Catal. B* **259**, 118090 (2019).
31. Li, Y. *et al.* Investigation of oxygen vacancy and photoluminescence in calcium tungstate nanophosphors with different particle sizes. *Mater. Res. Bull.* **50**, 36–41 (2014).
32. Kröger, F. & Vink, H. Relations between the concentrations of imperfections in crystalline solids. In *Solid State Phys.*, vol. 3, 307–435 (Elsevier, 1956).
33. Giannozzi, P. *et al.* Quantum espresso: A modular and open-source software project for quantum simulations of materials. *J. Phys. Condens. Matter.* **21**, 395502 (2009).
34. Vanderbilt, D. Soft self-consistent pseudopotentials in a generalized eigenvalue formalism. *Phys. Rev. B* **41**, 7892 (1990).
35. Payne, M. C., Teter, M. P., Allan, D. C., Arias, T. & Joannopoulos, A. J. Iterative minimization techniques for ab initio total-energy calculations: molecular dynamics and conjugate gradients. *Rev. Mod. Phys.* **64**, 1045 (1992).
36. Grimme, S. Accurate description of van der waals complexes by density functional theory including empirical corrections. *J. Comput. Chem.* **25**, 1463–1473 (2004).
37. Grimme, S. Semiempirical gga-type density functional constructed with a long-range dispersion correction. *J. Comput. Chem.* **27**, 1787–1799 (2006).
38. Rêgo, C. R. C., Oliveira, L. N., Tereshchuk, P. & Da Silva, J. L. F. Comparative study of van der Waals corrections to the bulk properties of graphite. *J. Phys. Condens. Matter.* **27**, 415502. https://doi.org/10.1088/0953-8984/27/41/415502 (2015).
39. Rêgo, C. R. C., Oliveira, L. N., Tereshchuk, P. & Da Silva, J. L. F. Corrigendum: Comparative study of van der Waals corrections to the bulk properties of graphite (2015 j. phys.: Condens. matter 27 415502). *J. Phys.: Condens. Matter***28**, 129501, https://doi.org/10.1088/0953-8984/28/12/129501 (2016).
40. Momma, K. & Izumi, F. Vesta 3 for three-dimensional visualization of crystal, volumetric and morphology data. *J. Appl. Cryst.* **44**, 1272–1276 (2011).
41. Rêgo, C. R. C. *et al.* SimStack: An intuitive workflow framework. *Front. Mater.*https://doi.org/10.3389/fmats.2022.877597 *(2022).*
42. Schaarschmidt, J. *et al.* Workflow engineering in materials design within the battery 2030+ project. *Adv. Energy Mater.* 2102638 (2021).
43. Rêgo, C. R. C. Kit-workflows/dft-qe: Dft-qe. https://github.com/KIT-Workflows/DFT-QE, https://doi.org/10.5281/ZENODO.7940876. (accessed May 16, 2023).
44. Wilkinson, M. D. *et al.* The FAIR guiding principles for scientific data management and stewardship. *Sci. Data*https://doi.org/10.1038/sdata.2016.18 *(2016).*

45. For information about the thermo_pw software:.
46. Bower, A. F. *Appl. Mech. Solids* (CRC Press, 2010).
47. Born, M. On the stability of crystal lattices. I. In *Mathematical Proceedings of the Cambridge Philosophical Society*, vol. 36, 160–172 (Cambridge University Press, 1940).
48. Mouhat, F. & Coudert, F.-X. Necessary and sufficient elastic stability conditions in various crystal systems. *Phys. Rev. B* **90**, 224104 (2014).
49. Nye, J. F. *Physical properties of crystals: Their representation by tensors and matrices* (Oxford university press, 1985).
50. Hill, R. The elastic behaviour of a crystalline aggregate. *Proc. Phys. Soc. A* **65**, 349 (1952).
51. Love, A. E. H. *A treatise on the mathematical theory of elasticity* (Cambridge university press, 2013).
52. Ranganathan, S. I. & Ostoja-Starzewski, M. Universal elastic anisotropy index. *Phys. Rev. Lett.* **101**, 055504 (2008).
53. Pugh, S. Xcii. relations between the elastic moduli and the plastic properties of polycrystalline pure metals. *Lond. Edinb. Dublin Philos. Mag. J. Sci.* **45**, 823–843 (1954).
54. Anderson, O. L. A simplified method for calculating the debye temperature from elastic constants. *J. Phys. Chem. Solids* **24**, 909–917 (1963).
55. Birch, F. The velocity of compressional waves in rocks to 10 kilobars: 1. *J. Geophys. Res.* **65**, 1083–1102 (1960).
56. Belomestnykh, V. N. The acoustical grüneisen constants of solids. *Tech. Phys. Lett.* **30**, 91–93 (2004).
57. Slack, G. Solid state physics: Advances in research and applications. vol. 34, 1 (Academic Press, New York, 1979).
58. Slack, G. A. Nonmetallic crystals with high thermal conductivity. *J. Phys. Chem. Solids* **34**, 321–335 (1973).
59. Morelli, D., Jovovic, V. & Heremans, J. Intrinsically minimal thermal conductivity in cubic I-V-VI 2 semiconductors. *Phys. Rev. Lett.* **101**, 035901 (2008).
60. Skoug, E. J., Cain, J. D. & Morelli, D. T. Structural effects on the lattice thermal conductivity of ternary antimony-and bismuth-containing chalcogenide semiconductors. *Appl. Phys. Lett.* **96**, 181905 (2010).
61. Shindé, S. L. & Goela, J. *High thermal conductivity materials*, vol. 91 (Springer, 2006).
62. Nielsen, M. D., Ozolins, V. & Heremans, J. P. Lone pair electrons minimize lattice thermal conductivity. *Energy Environ. Sci.* **6**, 570–578 (2013).
63. Xiao, Y. *et al.* Origin of low thermal conductivity in snse. *Phys. Rev. B* **94**, 125203 (2016).
64. Klemens, P. The scattering of low-frequency lattice waves by static imperfections. *Proc. Phys. Soc. A* **68**, 1113 (1955).
65. Klemens, P. Thermal resistance due to point defects at high temperatures. *Phys. Rev.* **119**, 507 (1960).
66. Callaway, J. & von Baeyer, H. C. Effect of point imperfections on lattice thermal conductivity. *Phys. Rev.* **120**, 1149 (1960).
67. Abeles, B. Lattice thermal conductivity of disordered semiconductor alloys at high temperatures. *Phys. Rev.* **131**, 1906 (1963).
68. Clarke, D. R. Materials selection guidelines for low thermal conductivity thermal barrier coatings. *Surf. Coat. Technol.* **163**, 67–74 (2003).
69. Peng, W., Petretto, G., Rignanese, G.-M., Hautier, G. & Zevalkink, A. An unlikely route to low lattice thermal conductivity: Small atoms in a simple layered structure. *Joule* **2**, 1879–1893 (2018).
70. Park, K., Mohamed, M., Aksamija, Z. & Ravaioli, U. Ab initio lattice dynamics and thermochemistry of layered bismuth telluride (bi2te3). *J. Appl. Phys.* **117**, 015103 (2015).
71. Peng, W. *et al.* Lattice hardening due to vacancy diffusion in (gete) msb2te3 alloys. *J. Appl. Phys.***126** (2019).
72. Emery, A. A. & Wolverton, C. High-throughput dft calculations of formation energy, stability and oxygen vacancy formation energy of ABO_3 perovskites. *Sci. Data* **4**, 1–10 (2017).
73. Boas, W. & Mackenzie, J. Anisotropy in metals. *Prog. Metal Phys.* **2**, 90–120 (1950).
74. Kern, H., Liu, B. & Popp, T. Relationship between anisotropy of p and s wave velocities and anisotropy of attenuation in serpentinite and amphibolite. *J. Geophys. Res.* **102**, 3051–3065 (1997).
75. Christensen, N. I. Serpentinites, peridotites, and seismology. *Int. Geol. Rev.* **46**, 795–816. https://doi.org/10.2747/0020-6814.46.9.795 (2004).
76. Shen, J. *et al.* Vacancy scattering for enhancing the thermoelectric performance of cugate 2 solid solutions. *J. Mater. Chem. A* **4**, 15464–15470 (2016).
77. Pei, Y. & Morelli, D. T. Vacancy phonon scattering in thermoelectric in2te3-insb solid solutions. *Appl. Phys. Lett.* **94**, 122112-1–122112-4 (2009).

Acknowledgements

H. Pecinatto thanks the Amazonas Research Support Foundation (FAPEAM). B. M. S. Perrone thanks the Brazilian Founding Agency – CAPES. C. A. Frota thanks the Geotechnical Research Group (GEOTEC) at the Federal University of Amazonas. Cicero Mota thanks the Federal University of Amazonas. M. S. S. Gusmão thanks the Federal University of Amazonas. H. O. Frota thanks the National Council for Scientific and Technological Development – grant number 311682/2021-9. A. C. Dias, D. Guedes-Sobrinho, and M. J. Piotrowski thanks Centro Nacional de Processamento de Alto Desempenho em São Paulo (CENAPAD-SP, UNICAMP/FINEP - MCTI project) for resources into the 897 and 570 projects and Lobo Carneiro HPC (NACAD) at the Federal University of Rio de Janeiro (UFRJ) for resources into 133 project. D. Guedes-Sobrinho thanks the CIMATEC SENAI at Salvador – BA, Brazil, for the partnership and support through the CIMATEC and Atos Computers, and "Laboratório Central de Processamento de Alto Desempenho" (LCPAD) financed by FINEP through CT-INFRA/UFPR projects. M. J. Piotrowski thanks the Rio Grande do Sul Research Foundation (FAPERGS) and National Council for Scientific and Technological Development – grant number 307345/2021-1. C. R. C. Rêgo and W. Wenzel thank the German Federal Ministry of Education and Research (BMBF) for financial support of the project Innovation-Platform MaterialDigital (www.materialdigital.de) through project funding FKZ no: 13XP5094A. The simulations were partially performed on the HoreKa supercomputer funded by the Ministry of Science, Research and the Arts Baden-Württemberg and the Federal Ministry of Education and Research. Authors also thank the resources of the "Laboratory of Material Simulation" at the Federal University of Amazonas (UFAM), the "Geotechnical Research Group" (GEOTEC), and the resources of the "Centro Nacional de Supercomputação (CESUP-UFRGS)"

Author contributions

C.A.F. and H.O.F. conceived the project, C.R.C.R., A.C.D., M.J.P., W.W., and C.M. provided the computing resources. H.O.F. and H.P. and C.R.C.R. performed the calculations. H.P., C.R.C.R., W.W., C.A.F., B.M.S.P., M.J.P., D.G.-S., A.C.D., C.M., M.S.S.G., and H.O.F. prepared the figures, and tables, wrote the manuscript, SI, analyzed the results, and reviewed the manuscript.

Funding
Open Access funding enabled and organized by Projekt DEAL.

Competing interests
The authors declare no competing interests.

Additional information
Supplementary Information The online version contains supplementary material available at https://doi.org/10.1038/s41598-023-44424-9.

Correspondence and requests for materials should be addressed to C.R.C.R.

Reprints and permissions information is available at www.nature.com/reprints.

Publisher's note Springer Nature remains neutral with regard to jurisdictional claims in published maps and institutional affiliations.